Journal of Materials Science: Materials in Electronics (2019) 30:17601–17611
https://doi.org/10.1007/s10854-019-02109-y

2D/3D interface engineering: direct Z-scheme g-C_3N_4/$YMnO_3$ heterojunction for reinforced visible-light photocatalytic oxidation

Yizhang Wu[1] · Xuan Zhou[1] · Mengmeng Li[1] · Yuanqi Wang[1] · Boye Zhou[1] · Niandu Wu[1] · Wei Zhong[1] · Hong-Ling Cai[1] · X. S. Wu[1]

Received: 11 July 2019 / Accepted: 27 August 2019 / Published online: 31 August 2019

Abstract

Graphitic carbon nitride (g-C_3N_4) is a two-dimensional (2D) photocatalyst, but it appears a mediocre catalytic property due to the recombination of charge carriers. Constructing heterojunctions can boost the separation and suppress the recombination of photo-generated electron–hole pairs. For the conventional Type-II heterojunction, the oxidation ability is significantly reduced due to the decreasing of band gap. We try to maintain its oxidation capacity and promote the artificial bandgap by tailoring a Z-scheme heterojunction through interface engineering. Herein, we grafted different proportions of $YMnO_3$ 3D-nanoparticles onto g-C_3N_4 2D-nanosheets. This special 2D/3D mixed-dimensional nanocomposite exhibits efficient charge carrier transport performance according to the electrochemistry and photocurrent measurement. The outstanding photocatalytic oxidation ability can be verified by the rate of Rhodamine B degradation, which is 3.8 and 2.3 times of $YMnO_3$ and g-C_3N_4, respectively. Theoretical calculation, active group capture experiments and electron spin resonance indicate the energy band position and the reactive groups (superoxide radicals and holes). The optimized g-C_3N_4/$YMnO_3$ heterojunction utilizes the interfacial synergistic effect to achieve a composition of vigorous oxidizing ability and outstanding visible light harvesting. This work will pave a promising access for mechanism and interface engineering of other g-C_3N_4-based Z-scheme heterojunctions.

1 Introduction

In the current situation of increasingly serious environmental pollution, the development of visible–light-driven photocatalyst is a project related to the quality of human future. Graphitic carbon nitride (g-C_3N_4) is a cost-effective, high-performance, no secondary polluting and human nontoxic photocatalyst [1] [2] [3]. However, the bulk g-C_3N_4 is not satisfactory in photocatalytic efficiency as a result of its excessive photo-generated electron hole recombination rate [4]. Forming heterojunctions with other different semiconductors can overcome these obstacles because g-C_3N_4 has flexible plasticity due to its own polymerization characteristics The g-C_3N_4-based semiconductor heterojunctions [5] [6] are usually classified into two categories: Type-II semiconductor heterojunction [7] [8] and Z-scheme heterojunction [9]. Although Type-II heterojunction structure can achieve efficient charge carriers separation, the conduction band (CB) positon is closed to the valence band position of each semiconductors [10], resulting in weak photo-generated electron reduction ability. In addition, the reduction of the band gap involved in the photocatalytic process results in an unsatisfactory photo-generated hole oxidizing ability [11].

To resolve the dilemma of narrow bandgap and weak oxidizing ability, Z-scheme heterojunctions have been developed. A Z-scheme heterojunction consists of three components: two narrow-bandgap semiconductors and a medium [12]. Remarkably, it promotes electron transportation and suppresses the reverse migration rate of charge carriers [13]. This model not only preserves the advantages of conventional Type-II heterojunctions [14], but also achieve improving light absorption and enhanced oxidizing properties.

Electronic supplementary material The online version of this article (https://doi.org/10.1007/s10854-019-02109-y) contains supplementary material, which is available to authorized users.

✉ Hong-Ling Cai
hlcai@nju.edu.cn

✉ X. S. Wu
xswu@nju.edu.cn

[1] Collaborative Innovation Center of Advanced Microstructures, Lab of Solid State Microstructures, School of Physics, Nanjing University, Nanjing 210093, People's Republic of China

However, the participation of the medium can easily lead to poor stability of the sample [15] [16]. Therefore, it is desirable to fabricate a direct Z-scheme heterojunction which benefits by the synergy of interfacial intimate contact.

Herein, we constructed a direct Z-scheme g-C_3N_4/$YMnO_3$ heterojunction by assembling a hybrid of g-C_3N_4 nanosheets and $YMnO_3$ nanoparticles for the flexible "chemical tailoring" [17] and a narrow bandgap. This novel g-C_3N_4/$YMnO_3$ heterojunction exhibits enhanced visible-light harvesting and excellent oxidizing ability by photocatalytic degradation. In addition, the sample has superior charge carrier mobility and inferior electron–hole recombination via Electrochemical Impedance Spectroscopy (EIS), Photoluminescence (PL) and photocurrent measurements. Furthermore, photo-cavities (h^+) and superoxide radicals ($\cdot O_2^-$) can be traced in the activated group capture tests, electron spin resonance (ESR) and different pH value experiment, which confirmed a direct Z-scheme g-C_3N_4/$YMnO_3$ heterojunction. Due to the construction of direct Z-scheme g-C_3N_4/$YMnO_3$ heterojunction, we successfully made a combination of enhanced visible-light absorption regulation and superior photocatalytic oxidation. This work also provides a novel approach to designing a mixed dimensional Van der Waals heterojunctions in new energy development and functionalized materials application.

2 Materials and methods

The reagents used were of analytical grade and did not require further purification. $YMnO_3$ was obtained by a sol–gel method using $Y(NO_3)_3{\cdot}6H_2O$ and $Mn(CH_3CO_2)_2{\cdot}4H_2O$. G-$C_3N_4$ was obtained by heating melamine at 550 °C for 2 h in a muffle furnace. The Z-scheme photocatalyst g-C_3N_4/$YMnO_3$ was obtained by simple hydrothermal treatment. Typically, 665 mg of g-C_3N_4 sample and 35 mg of $YMnO_3$ were dispersed into 30 mL of deionized water with the assistance of ultrasonication for 30 min, respectively. Then, the $YMnO_3$ suspension solution was added dropwise into the g-C_3N_4 suspension solution with constant stirring. Subsequently, the solution was vigorously stirred for 5 h at room temperature. The obtained suspensions solution was heated to 110 °C to remove the water. After that, the solid product was dried at 110 °C for 6 h in oven, followed by milling and calcination at 550 °C in a muffle furnace for 1 h in a semi-closed system at a heating rate of 10 °C min^{-1} under air condition. The product was washed for several times with distilled water and absolute ethanol and then dried at 80 °C for 10 h. The obtained products were denoted as g-C_3N_4/$YMnO_3$ (x %), where x stands for the theoretical mass percent of $YMnO_3$ in the g-C_3N_4/$YMnO_3$ composite. The as-obtained sample was also denoted as g-C_3N_4/$YMnO_3$ (5 wt%). Similarly, the g-C_3N_4/$YMnO_3$ (10 wt%), g-C_3N_4/$YMnO_3$ (20 wt%) and g-C_3N_4/$YMnO_3$ (30 wt%) were prepared following the procedure mentioned above.

The X-ray diffraction (XRD) was measured by a Rigaku Ultima III diffratometer with $Cu-K\alpha$ radiation ($\lambda = 1.54056$ Å), operated in θ–2θ configuration. The transmission electron microscope (TEM) was recorded by Model JEOL-2010. Scanning electron microscopy (SEM) was an Ultra-high resolution scanning electron microscope, model Gemini-SEM 500. The X-ray photoelectron spectroscopy (XPS) test was an instrument-using model the PHI 5000 VersaProbe of UlVAC-PHI. Fourier-transformed infrared (FT-IR) spectra were performed by using a NEXUS870 spectrometer with KBr pellets in the range of 500–4000 cm^{-1}. The UV–Vis diffuse reflectance spectra of the as-obtained samples were obtained by using a Hitachi UV-3000 spectrophotometer with a BaSO4-coated integrating sphere. Photoluminescence (PL) spectra the as-obtained samples were obtained by Horiba HR800 with an excitation wavelength of 488 nm. Electrochemical Impedance Spectroscopy (EIS) were carried out using a CHI660E electrochemical workstation with a three-electrode system (Chenhua Instruments, China). In this system, the resultant electrode, platinum wire and Ag/AgCl were used as the working electrode, counter electrode and reference electrode, respectively. The working electrode was prepared as following: 5 mg of the as-obtained photocatalyst powders and 20 μL of 0.25% Nafion solution were added into 2 mL of absolute ethanol to make a slurry, then the mixture solution was ultrasound for 2 h. 200 μL of the obtained suspension was uniformly spread onto a 1×1 cm^{-1} fluorine-doped tin-oxide (FTO) glass substrate with the side protected by Scotch tape. After the infrared lamp drying, the working electrode was further dried at 80 °C for 12 h to obtain the final working electrode. A 0.5 mol L^{-1} sodium sulfate aqueous solution was used as the electrolyte. A 300 W Xe lamp was used as the visible light source with a 420 nm cutoff filter ($\lambda > 420$ nm). The electrochemical impedance spectroscopy (EIS) frequency ranged from 0.1 to 100000 Hz in parallel with the alternating current signal amplitude of 5 mV. The Brunauer–Emmett–Teller (BET) surface area and pore size distribution of the as-obtained samples were measured by N_2 adsorption–desorption isotherms using an ASAP 2010 analyzer (Micromeritics, USA) at 77 K. The photocatalytic degradation experiment was performed using a 300 W xenon lamp source, Model Perfectlight-PLS-SXE300C. The initial concentration of Rhodamine B was 0.01 mmol/L, and 50 mg of the sample was mixed with 50 mL of this concentration of Rhodamine B solution for photocatalytic degradation experiments.

3 Result and discussion

3.1 Characterization of photocatalyst

X-ray diffraction (XRD) patterns of heterojunction with pure g-C_3N_4 [18] and $YMnO_3$ [19] were obtained as shown in Fig. 1. In detail, the diffraction peaks at 2θ = 13.0° and 2θ = 27.4° are two distinct characteristic peaks of g-C_3N_4 of (100) and (002) plane [20], respectively. In addition, some characteristic peaks of $YMnO_3$ at 2θ = 15.7°, 29.1°, 30.1°, 43.4°, 51.5°, 57.1°, 60.7°, 61.7° and 62.4° appear in the XRD pattern, corresponding to (200), (110), (111), (004), (112), (114), (300), (116), (221), (215) and (222) diffractions [21] [22], respectively. It illustrates that g-C_3N_4/$YMnO_3$ hybrids synthesized by sol–gel don't have any impurity phase. Furthermore, the peak intensity of g-C_3N_4 gradually decreases when the ratio of the $YMnO_3$ content increases. Due to the addition of $YMnO_3$, the mesopores of g-C_3N_4 were blocked by $YMnO_3$ nanoparticles, causing the gradually ascending intensity of the $YMnO_3$ (112) peak in the g-C_3N_4/$YMnO_3$ heterojunction. These confirm that g-C_3N_4 and $YMnO_3$ coexisted in the composite, and g-C_3N_4/$YMnO_3$ hybrids were successfully constructed.

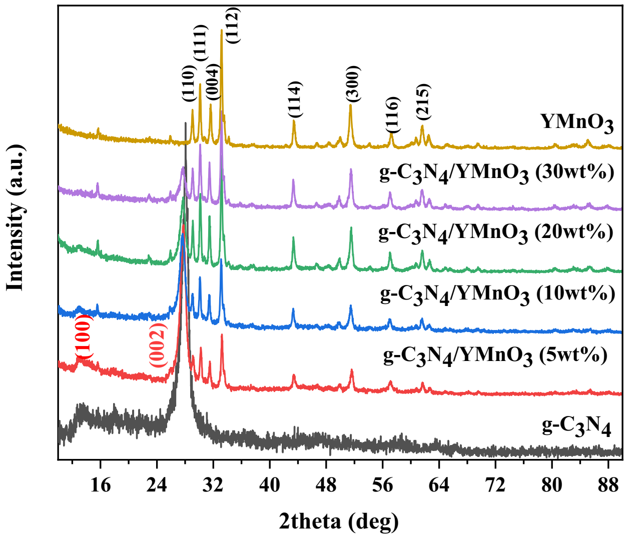

Fig. 1 X-ray diffraction patterns of pure g-C_3N_4, $YMnO_3$ and g-C_3N_4/$YMnO_3$ hybrids with different $YMnO_3$ concentration

To further explore the spatial structure and surface properties of heterojunctions, Fourier transform infrared (FTIR) spectroscopy were performed as shown in Fig. 2. Peaks at 1253, 1328, 1417, 1465, 1568 and 1635 cm^{-1} of pristine g-C_3N_4 are corresponding to C = N and C–N, which is consistent with previous reports [23] [24]. The strong band at 808 cm^{-1} is attributed to the breathing pattern characteristic of the tri-s-triazine units [25]. A peak located at 701 cm^{-1} is the characteristic peak of $YMnO_3$ [26] [27]. Notably, this unique peak was always presented in the g-C_3N_4/$YMnO_3$ hybrid, and the intensity of this peak changes with the concentration of $YMnO_3$. It indicates that g-C_3N_4 nanosheets completely contact with $YMnO_3$ nanoparticles. The characterization of hybrids changes with the increase of $YMnO_3$ concentration [28] [29]. The FTIR spectroscopy results well demonstrate that $YMnO_3$ was successfully anchored to the surface to form a heterojunction.

The absorption intensity of visible light acts as an important criterion in evaluating the activity of photocatalysis [30]. Thus, the optical response characteristics of pristine g-C_3N_4, $YMnO_3$ and the hybrids are measured by UV–Vis diffuse reflectance spectra (DRS). As shown in Fig. 2b, the absorption range of g-C_3N_4 is corresponding to the band gap excitation, which locates at 460 nm in consistence with previous reports [31] [32]. Compared to bulk g-C_3N_4 [33], the series of hybrids exhibit an enhanced light harvesting due to the interaction between $YMnO_3$ nanoparticles and g-C_3N_4 nanosheets, which allows more charge carriers to improve the photocatalytic activity.

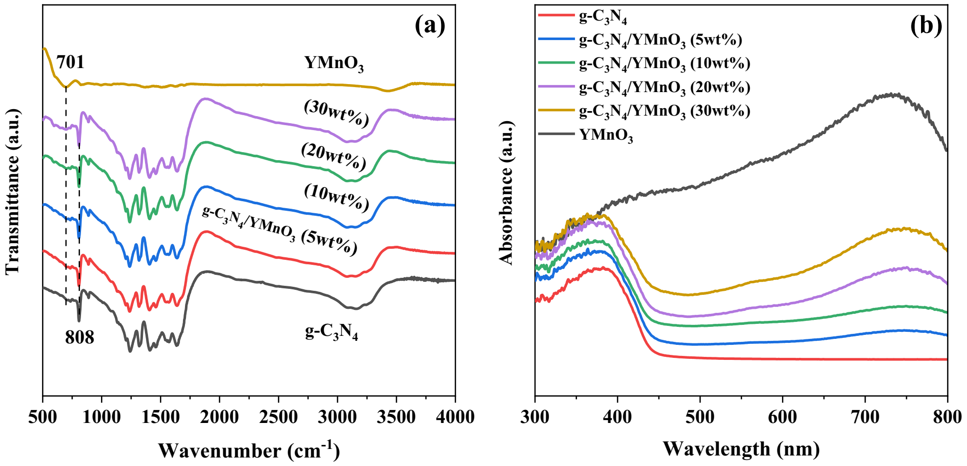

Fig. 2 **a** FTIR spectra and **b** UV–Vis DRS of the as-obtained pure g-C_3N_4, pristine $YMnO_3$ and g-C_3N_4/$YMnO_3$ hybrids

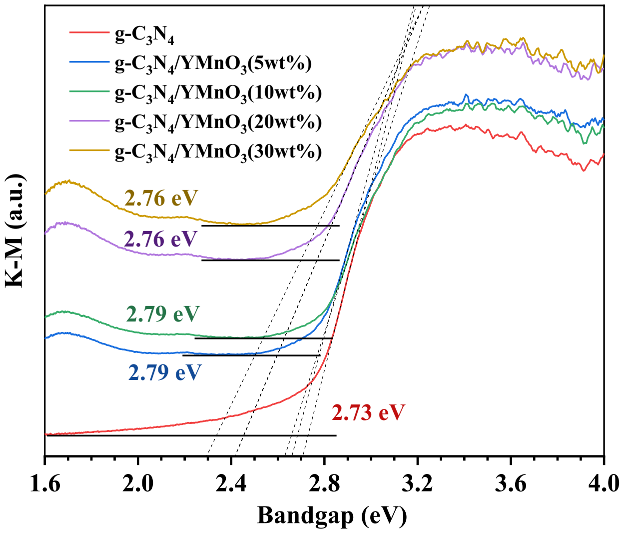

Fig. 3 The transformed Kubelka–Munk function spectrum

The bandgap is a significantly index to evaluate the potential of a heterojunction. The corresponding transformed Kubelka–Munk function spectrum of DRS presents the variation tendency with different concentration of $YMnO_3$ as shown in Fig. 3. In detail, compared with the bulk $g\text{-}C_3N_4$, heterojunctions all take superior performance, elevating from 2.73 to 2.79 eV. Contrasting with the reduction of the band gap in conventional Type-II heterojunctions, it is a potent proof to confirm the construction of a direct Z-scheme heterojunction [34] [35].

In order to elucidate the interfacial interaction, the chemical composition and element valence state of the $g\text{-}C_3N_4/YMnO_3$ hybrids, X-ray photoelectron spectroscopy (XPS) characterization had been carried out (Figs. 4 and S1). The high resolution C1s and N1s XPS spectra of $g\text{-}C_3N_4$ and C1s, N1s, Y 3d, Mn 2p and O1s XPS spectra of $g\text{-}C_3N_4/YMnO_3$ (10 wt%) have been analyzed, respectively. The high-resolution XPS spectra of pure $g\text{-}C_3N_4$ C1s can be

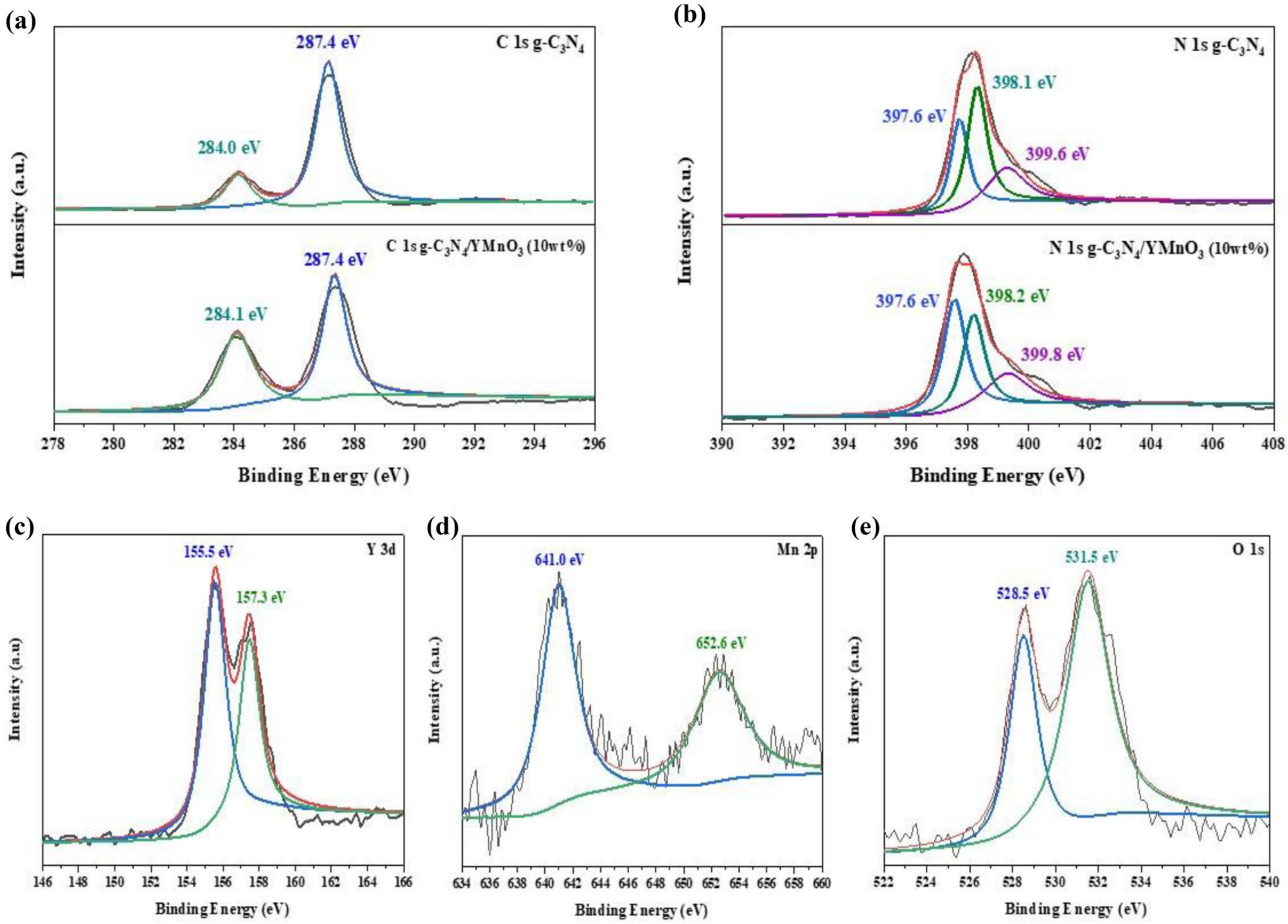

Fig. 4 XPS spectra **a**–**e** of C 1s, N 1s, Y 3d, Mn 2p, and O 1s, respectively, for $g\text{-}C_3N_4$ and $g\text{-}C_3N_4/YMnO_3$

fitted to two main peaks of 284.0 eV and 287.4 eV (Fig. 4a), respectively, which are attributed to the sp^2 C–C bond and N–C = N [36] in the g-C_3N_4 aromatic ring. N1s peak of g-C_3N_4 (Fig. 4b) is fitted to three peaks at positions of 397.6 eV, 398.1 eV and 399.6 eV, respectively, which can be regarded as C–N = C bond, N–$(C)_3$ bond and C–N–H bond [37]. The peaks of $3d_{5/2}$ and $3d_{3/2}$ of yttrium with positions 155.5 eV and 157.3 eV have been shown in Fig. 4c, and their band splitting $\Delta = 1.8$ eV is consistent with those reported in the literatures [38]. The high resolution spectrum of Mn 2p (Fig. 4d) for g-C_3N_4/$YMnO_3$ (10 wt%) sample is well fitted into two main peaks at 641.0 eV and 652.6 eV, corresponding to the binding energies of Mn $2p_{3/2}$ and $2p_{1/2}$, respectively, indicating that Mn mainly exhibits +3 oxidation state [39]. It can be seen that the asymmetric peaks of O1s are respectively decomposed into two peaks centered on 528.5 eV and 531.5 eV (Fig. 4e). The former is related to the lattice oxygen content, and the latter is related to the chemical adsorption oxygen on the hybrid product. It not only further confirms the synthesis of g-C_3N_4/$YMnO_3$ heterojunctions, but also proves the existence of a vigorous interaction via a mixed dimensional Van der Waals heterojunctions or a g-C_3N_4-based heterojunction.

The morphologies of g-C_3N_4, $YMnO_3$ and g-C_3N_4/$YMnO_3$ (10 wt%) composites (Fig. 5) were observed by scanning electron microscopy (SEM) and transmission electron microscopy (TEM). The pristine g-C_3N_4 (Fig. 5a) exhibits a layered structure with more wrinkles and irregular stacking, whose surface is relatively smooth. This was also confirmed by the TEM (Fig. 5d–f), where g-C_3N_4 was a typical two-dimensional nanosheets structure. The SEM image of pristine $YMnO_3$ nanoparticles (Fig. 5b) shows granular morphology of the irregular agglomerated nanoparticles. As shown in Fig. 5c, $YMnO_3$ nanoparticles are randomly attached to the surface of g-C_3N_4 nanosheets. In addition, the detailed morphology of 10 wt% hybrid is further investigated by high resolution TEM (HRTEM). The darker spherical particles in Fig. 5d and e are $YMnO_3$ nanoparticles, which are well dispersed on the surface of the g-C_3N_4 nanosheet. The lattice fringes with d-spacing of 0.303 nm and 0.391 nm, which corresponds to the (110) and (112) plane of hexagonal phase $YMnO_3$ ($P6_3cm$) [39]. A clear grain boundary can be observed, which indicates that a heterojunction interface is formed in g-C_3N_4/$YMnO_3$ hybrids. Textural properties of the as-obtained samples also can be obtained by Brunauer–Emmett–Teller (BET) measurement (Fig.S2 and Table. S1).

Photoluminescence(PL) spectra of g-C_3N_4 and g-C_3N_4/$YMnO_3$ hybrids have been tested at an excitation wavelength of 488 nm (Fig. 6a).The surface state and oxygen vacancy information of the sample can reflect the photocatalytic activity by the PL spectrum [40] [41]. Generally, the intensity of PL signal and charge recombination rate are positively correlated. The lower PL intensity usually represents the lower electron–hole pairs recombination rate [42] [43].

The PL intensity of g-C_3N_4/$YMnO_3$ hybrids has a significant decrease compared to pure g-C_3N_4 (Fig. 6a), which indicates that the composite Z-scheme heterojunctions could

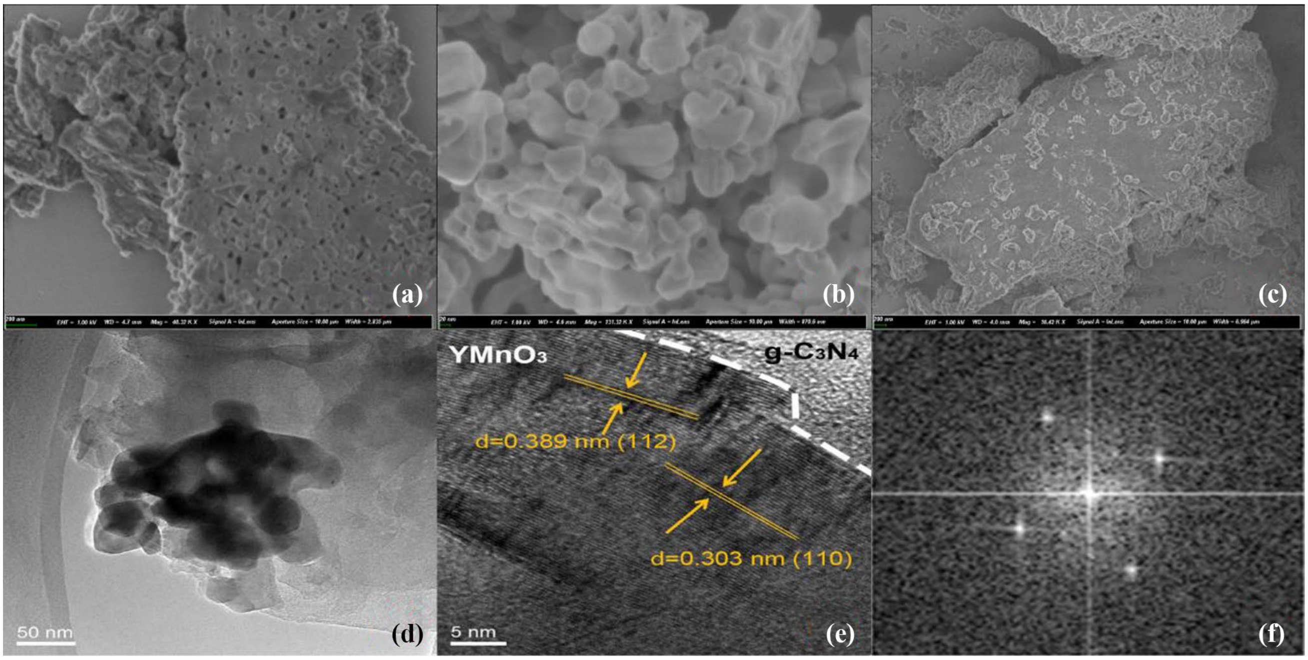

Fig. 5 SEM images of g-C_3N_4 (**a**), $YMnO_3$ (**b**) and g-C_3N_4/$YMnO_3$ (10 wt%) (**c**);TEM images of g-C_3N_4/$YMnO_3$ (10 wt%) with different resolutions (**d**–**e**); partial Fast Fourier transform (FFT) image (**f**)

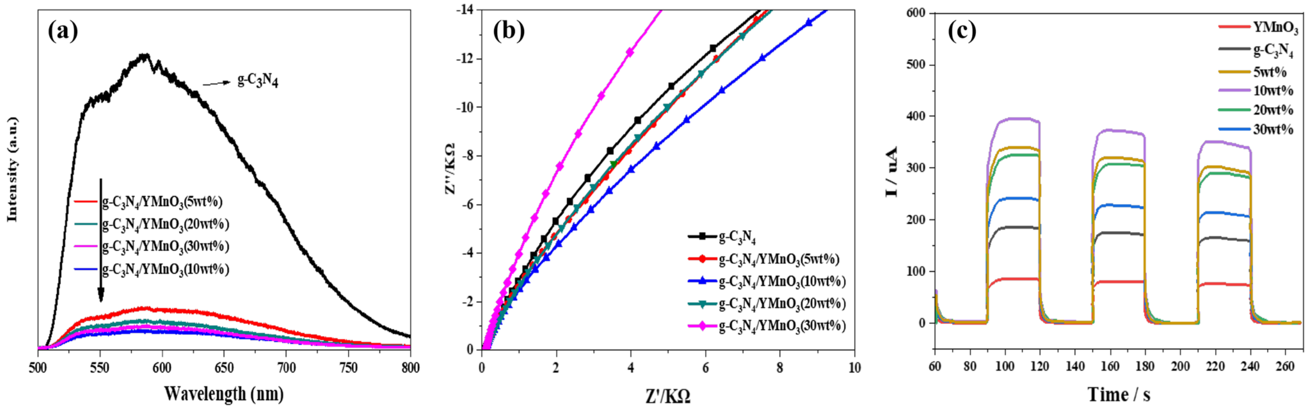

Fig. 6 PL spectra **a**, EIS **b** and TPR **c** results of the catalysis

effectively suppress the recombination of electron–hole pairs [44]. In addition, the PL intensity of the g-C_3N_4/$YMnO_3$ hybrids has the lowest value at the concentration of 10 wt%. It illustrates that excess $YMnO_3$ nanoparticles act as the recombination center of photo-generated carriers.

The EIS results of samples are presented in Fig. 6b. In detail, the arc is inversely proportional to the interface charge transfer efficiency and the separation efficiency of photo-generated electron holes [45] [46]. It can be explained by the following formulas:

$$z' = \frac{R}{1 + (\omega Rc)^2} \tag{1}$$

$$z'' = -\frac{\omega R^2 C}{1 + (\omega RC)^2} \tag{2}$$

$$\left(z' - \frac{R}{2}\right)^2 + z''^2 = \left(\frac{R}{2}\right)^2 \tag{3}$$

According to the formulas, the magnitude of the resistance can be understood as the charge transfer rate. The intensity of the EIS curve of g-C_3N_4/$YMnO_3$ (10 wt%) is lower than that of pure g-C_3N_4 and any other concentrations, which proves that g-C_3N_4/$YMnO_3$ (10 wt%) performs a more efficient separation of photo-generated electron–hole pairs [47]. As can be seen in Fig. 6c, it depicted transient photocurrent response (TPR) for pristine g-C_3N_4, $YMnO_3$ and g-C_3N_4/$YMnO_3$ hybrids under visible-light irradiation. As we known, a larger photocurrent density exhibits a higher segregation efficiency of the photogenerated charge carriers [48]. It was clearly observed that steady and reproducible photocurrent responses were observed for all the samples during two on–off intermittent irradiation cycles. Obviously, it could be seen that the g-C_3N_4/$YMnO_3$ (10 wt%) hybrid illustrated the largest photocurrent intensity among all the sample, which was almost 2.1 and 4.6 times larger than those of pure g-C_3N_4 and $YMnO_3$, respectively, which could be attributed to the existence of a strong interface interaction between g-C_3N_4 and $YMnO_3$, where the photogenerated electrons and holes could be efficiently separated in space and the photoinduced charge carriers recombination could be effectively suppressed. This clearly revealed the loading of $YMnO_3$ accelerated the transfer and separation of the photogenerated electrons and holes of pure g-C_3N_4.

3.2 Photocatalytic performance for Rhodamine B degradation

The photocatalytic degradation of different concentrations of hybrids under visible light ($\lambda > 420$ nm) had been evaluated by degrading organic dye Rhodamine B (RhB) [49]. The photocatalytic properties of pristine g-C_3N_4 and $YMnO_3$ were also studied as the control experiments under the same experimental conditions. The photocatalytic activity of the different samples was obtained at the same irradiation time, as illustrated in Fig. 7a. $YMnO_3$ and g-C_3N_4 both have lower photocatalytic activities of 71.4% and 52.3%, owing to their rapid recombination rates of photo-generated electrons and holes. The degradation percentages of RhB using g-C_3N_4/$YMnO_3$ (5 wt%, 10 wt%, 20 wt% and 30 wt%) are obtained 34.3%, 23.1%, 45.4% and 57.5%, respectively.

To evaluate quantitatively the catalyst activity of photodegradable RhB, we used the first-order kinetic equation to fit the experimental data to get the degradation rate of different photo-catalysts as following [50]:

$$-\ln\left(C/C_0\right) = kt \tag{4}$$

where C_0 and C are the concentrations of RhB at the initial time and final time t, respectively, and k is the first-order degraded rate constant (min^{-1}) [51]. Pristine g-C_3N_4 and bare $YMnO_3$ decompose RhB at a rate of $k = 0.00549\ \text{min}^{-1}$ and $k = 0.00314\ \text{min}^{-1}$, respectively (Fig. 7b). The most

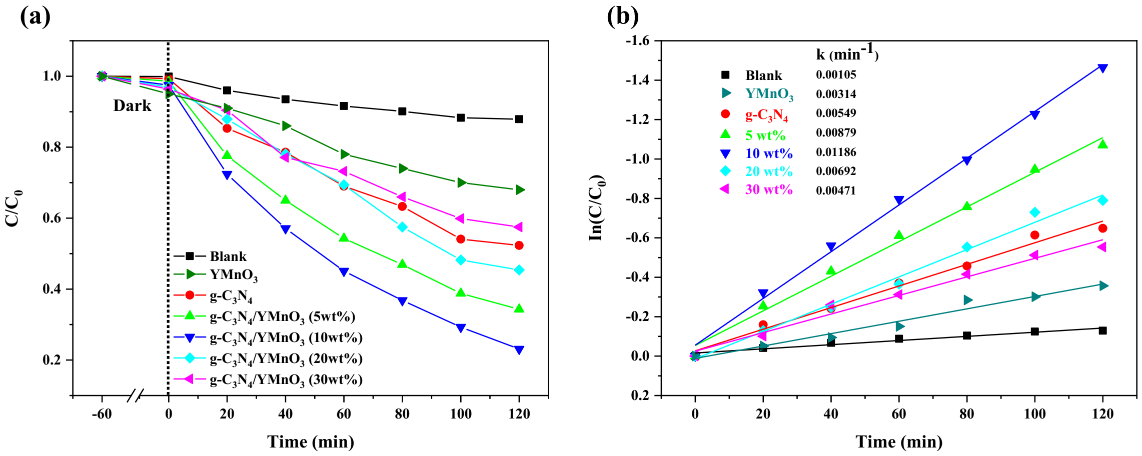

Fig. 7 **a** Photocatalytic performance for degradation of Rhodamine B **b** first-order kinetic equation

Table 1 Summary of photocatalytic performance for Rhodamine B degradation

Sample	Degradation of rhodamine B (%)	First-order kinetic equation (k min^{-1})
YMnO$_3$	0.701	0.00314
g-C$_3$N$_4$	0.523	0.00549
g-C$_3$N$_4$/YMnO$_3$ (5 wt%)	0.343	0.00879
g-C$_3$N$_4$/YMnO$_3$ (10 wt%)	0.231	0.01186
g-C$_3$N$_4$/YMnO$_3$ (20 wt%)	0.454	0.00692
g-C$_3$N$_4$/YMnO$_3$ (30 wt%)	0.575	0.00471

efficient g-C$_3$N$_4$/YMnO$_3$ (10wt %) degradation rate is k = 0.01186 min^{-1}, which is 2.3 times more than g-C$_3$N$_4$ and 3.8 times of bare YMnO$_3$, respectively. Therefore, the formation of this direct Z-scheme heterojunction can effectively enhance the oxidation ability [52]. The degradation rate of RhB degraded from g-C$_3$N$_4$, YMnO$_3$ and the hybrids obtained in the experiment are summarized in Table 1.

The recyclability and stability are some of the most important factors for water treatment applications. Hence, the performance over four consecutive cycles was tested and the XRD patterns before and after the reactions were compared to evaluate the recyclability and stability of the photocatalyst. As seen in Fig. 8a, only a small degree of deactivation of the g-C$_3$N$_4$/YMnO$_3$ (10 wt%) composite is observed after four consecutive cycles, which implies the great recyclability of the photocatalyst. At the same time, hardly any obvious changes in the peaks of the XRD patterns occur, which illustrates the stability of the photocatalyst (Fig. 8b). In summary, the heterojunction composite has good cyclability and a stable crystal structure.

3.3 Photocatalytic degradation mechanism

The ability of reducing and oxidizing in g-C$_3$N$_4$/YMnO$_3$ hybrids had been measured to elucidate the photocatalytic mechanism by different scavengers. The main active substances directly involved in the g-C$_3$N$_4$/YMnO$_3$ photocatalytic system are determined by active substance capture experiments (Fig. 9a). The degradation of RhB was tested in presence of different scavengers using g-C$_3$N$_4$/YMnO$_3$ (10 wt%) as the reference sample. Disodium edetate (Na$_2$-EDTA) [53], isopropanol (IPA) [54] and benzoquinamide (BZQ) [55] were used as photo-cavity (h$^+$), hydroxyl radicals (·OH) and superoxide radicals (·O$_2$$^-$) scavenger, respectively. The addition of IPA has no distinct effect on the degradation efficiency of RhB, eliminating the ·OH [56]. However, with BZQ as the ·O$_2$$^-$ scavenger, the photoinduced degradation rate significantly reduced to 62%. Furthermore, to confirm that ·O$_2$$^-$ is possibly generated during the photocatalytic process, a nitrogen purge experiment was carried out in order to eliminate the existence of oxygen [57]. As expected, the efficiency of heterojunction degradation of RhB is reduced to 56%. Similar to the above, when Na$_2$-EDTA was added, the degradation of RhB is greatly inhibited to 65%, indicating that h$^+$ also acts as a catalytic active group in photocatalytic. Therefore, the enhanced photocatalytic performances of hybrids can be explained by the Z-scheme g-C$_3$N$_4$/YMnO$_3$ heterojunction [58] that facilitated the generation and migration of h$^+$ and ·O$_2$$^-$.

Furthermore, we analyze the effect of pH value in RhB degradation. Generally, pH value affects the photocatalytic reaction by changing the surface charge and the adsorption behavior or by changing the generation of radicals [59]. With a decrease of pH value from 11 to 3, the adsorption capacity of g-C$_3$N$_4$/YMnO$_3$ remains constant, ruling out the former effect, while the photocatalytic activity improves

Table 2 X, E_{CB}, E_{VB} of g-C_3N_4 and $YMnO_3$

Samples	X (eV)	E_{CB} (eV)	E_{VB} (eV)
g-C_3N_4	4.72	− 1.12	1.56
$YMnO_3$	5.51	0.26	1.77

X ($YMnO_3$) = $(3.19*3.72*7.54^3)^{1/(1+1+3)}$

continuously (Fig. 9b). Based on the formation paths of ·OH (i.e. $h^+ + H_2O \rightarrow \cdot OH + H^+$ or $h^+ + OH^- \rightarrow \cdot OH$) [60] [61], a higher pH value favors the conversion of holes to ·OH. In the absence of Na_2-EDTA, the sample at pH of 3 shows much higher activity than at pH of 11. Since the activity of hydroxyl radicals is negligible, the degradation of RhB is mainly contributed by holes and superoxide radicals. It is evident that the hole concentration is much higher at pH of 3 than at pH of 11, while the concentration of superoxide radicals does not depend on the pH value. Therefore, the declined activity in basic solutions strongly support our expectation that the produced ·OH are not active for the RhB degradation reaction.

In addition, the CB and VB position of two semiconductors exert an important influence and play a decisive role in

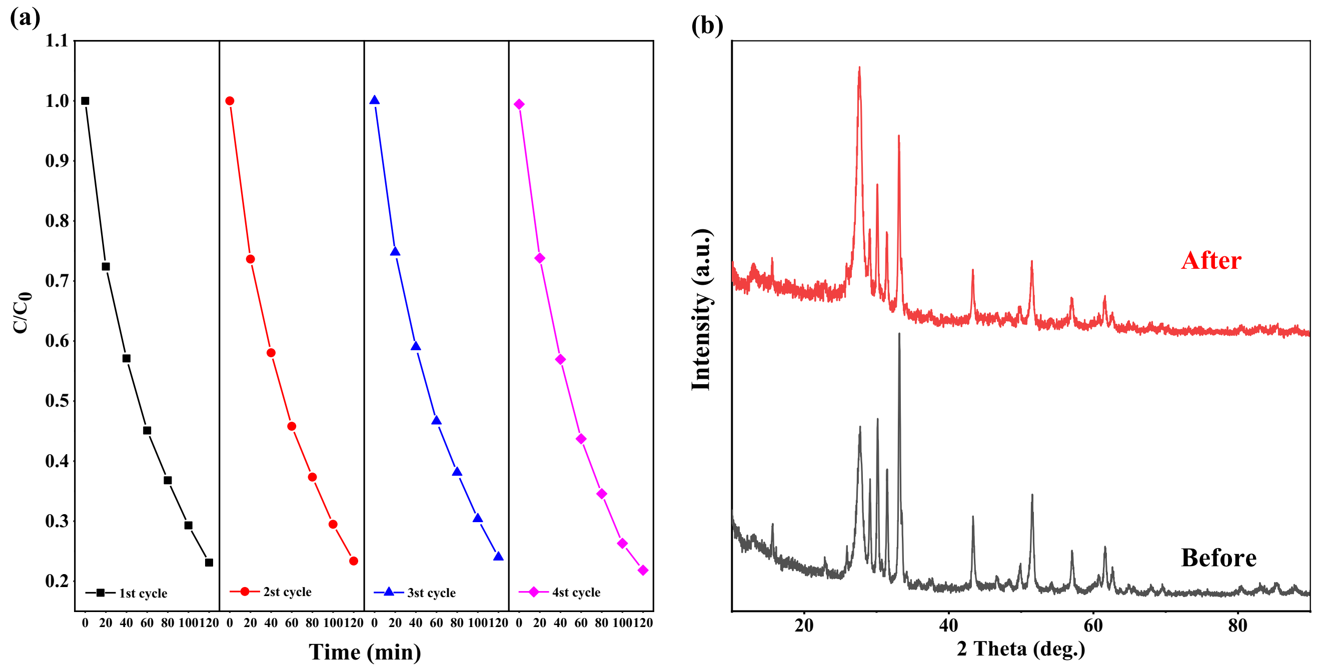

Fig. 8 Four photocatalytic degradation cycles (**a**) and the XRD patterns before and after the four reaction cycles (**b**)

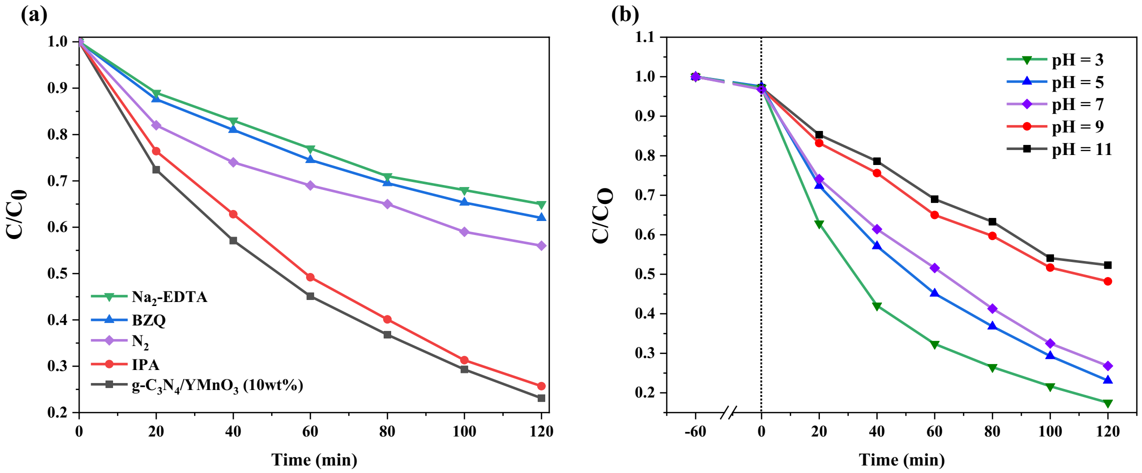

Fig. 9 Photocatalytic active substance capture with different scavengers (**a**) The effect of pH value in Rhb degradation (**b**)

photocatalytic mechanism [62]. Therefore, we calculated the energy band from the experimental g-C_3N_4 and $YMnO_3$ using the following three formulas:

$$\alpha h\nu = A\left(h\nu - E_g\right)^{n/2} \tag{5}$$

$$E_{CB} = X - E_e + 0.5E_g \tag{6}$$

$$E_{VB} = E_{CB} + E_g \tag{7}$$

The E_g of g-C_3N_4 and $YMnO_3$ is 2.69 eV and 1.51 eV by $E_g = 1240/h\nu$, respectively. The values n of $YMnO_3$ [63] and g-C_3N_4 [64] are both 1. The absolute electronegativity X of g-C_3N_4 is 4.72 eV. X for $YMnO_3$ can be calculated from the absolute electronegativities [65] of yttrium (3.19 eV), manganese (3.72 eV) and oxygen (7.54 eV). X, E_{CB} and E_{VB} corresponding to g-C_3N_4 and $YMnO_3$ can be summarized into Table 2.

To further explore the photocatalytic mechanism, electron spin resonance (ESR) was tested. As shown in Fig. 10, g-C_3N_4/$YMnO_3$ has a higher production efficiency of both radicals compared with pristine CN, in line with its higher photocatalytic activity. To understand this phenomenon, the energy diagram of this heterojunction is prepared.

According to bandgaps and the valence band positions, obtained from UV vis DRS and XPS-VB, respectively, CN has a conduction band of −1.12 eV and a valence band of 1.56 eV, while $YMnO_3$ has a conduction band of 0.26 eV and a valence band of 1.77 eV. Generally, $\cdot O_2^-$ is produced via a reduction of O_2 with the photogenerated electrons ($e^- + O_2 \rightarrow \cdot O_2^-$· $O_2/\cdot O_2^- = -0.33$ eV vs. NHE). The conduction band electrons in $YMnO_3$ are thermodynamically not active to produce $\cdot O_2^-$ (Fig. 10a). Thus, the higher concentration of $\cdot O_2^-$ in the g-C_3N_4/$YMnO_3$ system indicates a better accumulation of electrons in the conduction band of CN, rather than $YMnO_3$.

In terms of ·OH, it can be either directly produced by an oxidation of H_2O with holes ($h^+ + H_2O \rightarrow \cdot OH + H^+$) or come indirectly from $\cdot O_2^-$ through a series of reactions ($\cdot O_2^- + H_2O \rightarrow H_2O_2 \rightarrow \cdot OH$). Since the valence band of g-C_3N_4 (i.e. 1.56 eV) is not positive enough to produce ·OH directly, the ·OH observed in the pristine CN system (Fig. 10b) should be produced through the indirect path. The significantly higher concentration of ·OH in the presence of $YMnO_3$ is due to a change of the reaction path, to a direct oxidation of H_2O by the highly oxidative holes in the valence band of $YMnO_3$ ($h^+ + H_2O \rightarrow \cdot OH + H^+$). Therefore, the accumulation of electrons in the conduction band of CN while holes in the valence band of $YMnO_3$ highly suggests a Z-Scheme type charge transfer (Fig. 11a). Under the light irradiation, both $YMnO_3$ and g-C_3N_4 are excited. The photoelectrons in the conduction band of $YMnO_3$ tend to recombine with the holes in the valence band of g-C_3N_4. The left electrons in the conduction band of g-C_3N_4 are relatively stable thus continuously reduce O_2 to $\cdot O_2^-$. The holes in the valence band of $YMnO_3$ partially contribute to the oxidation of dyes, while the rest holes are converted to ·OH, which however is not reactive for RhB. In term of a conventional Type-II heterojunctions, the charge transfer from the high energy conduction band and valence band to the lower energy ones will lead to a decline of both $\cdot O_2^-$ and ·OH concentrations (Fig. 11b), which however is not the case of the g-C_3N_4/$YMnO_3$ system.

In general, in the Z-scheme heterojunction, light-induced electrons tend to transfer from $YMnO_3$ to g-C_3N_4 via the heterostructure interface [66]. Afterwards, electrons accumulate

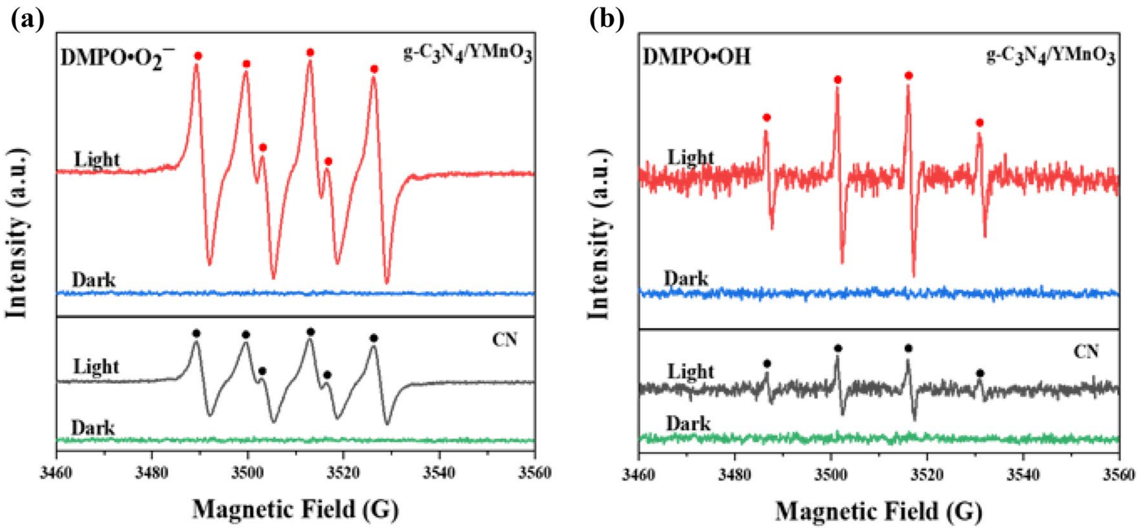

Fig. 10 ESR detections of **a** $\cdot O_2^-$ and **b** ·OH either in dark or after a light irradiation for 15 min

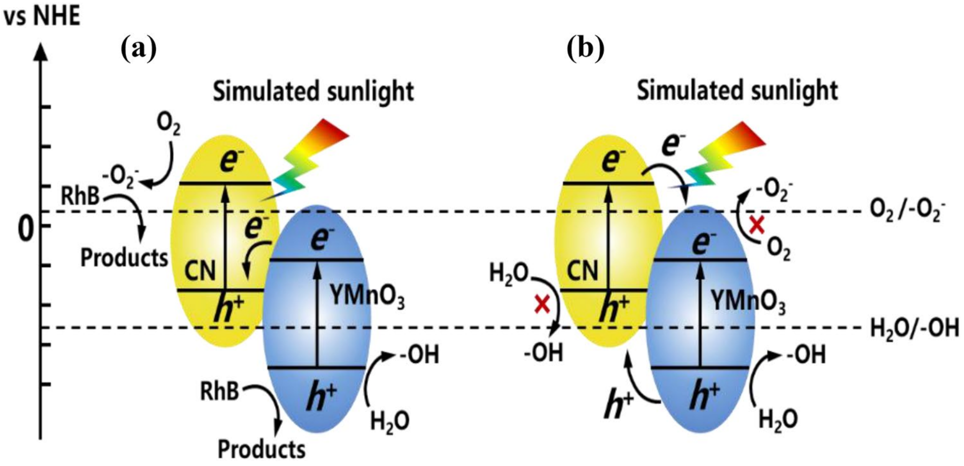

Fig. 11 **a** Z-Scheme charge transfer; **b** conventional charge transfer

in the CB of g-C_3N_4, and the holes are thus retained in the VB of $YMnO_3$, as shown in Fig. 12.

The production of h^+ and $\cdot O_2^-$ active materials increased photocatalytic oxidation ability and provided evidence of direct Z-scheme heterojunctions. We can express the migration and recombination process of photo-generated electron hole pairs by the following chemical formula:

$$g-C_3N_4/YMnO_3+hv \rightarrow g-C_3N_4\left(e^-+h^+\right)+YMnO_3\left(e^-+h^+\right) \tag{8}$$

$$\begin{aligned} & g-C_3N_4\left(e^-+h^+\right)+YMnO_3\left(e^-+h^+\right) \\ & \rightarrow g-C_3N_4(e^-)+YMnO_3\left(h^+\right) \end{aligned} \tag{9}$$

$$g-C_3N_4(e^-)+O_2 \rightarrow \cdot O_2^-+g-C_3N_4 \tag{10}$$

$$YMnO_3\left(h^+\right)+\text{Rhodamine B} \rightarrow YMnO_3+H_2O+CO_2 \tag{11}$$

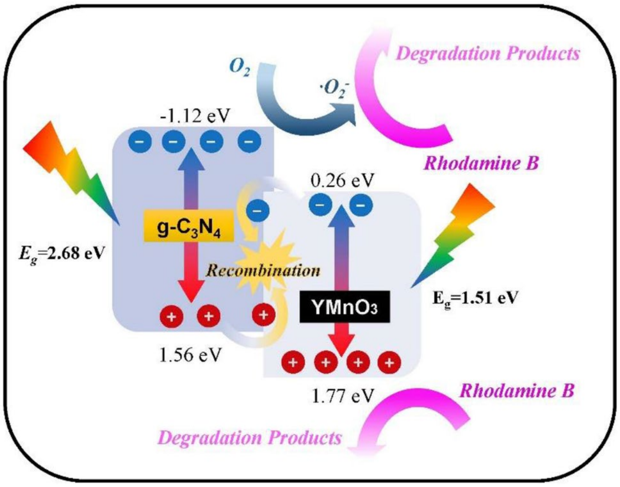

Fig. 12 Schematic illustration of charge generation and separation of Z-scheme hybrids

$$\cdot O_2^-+\text{Rhodamine B} \rightarrow H_2O+CO_2 \tag{12}$$

4 Conclusion

In this work, we have implemented a 2D/3D interfacial engineering to boost oxidizing ability and visible light harvesting by constructing g-C_3N_4/$YMnO_3$ heterojunctions. UV–vis DRS confirmed the promoting of visible-light adsorption and the extensive bandgap. In addition, EIS, PL and transient photocurrent measurement demonstrated superior charge carrier migration rate and inferior photogenerated electron and holes. Furthermore, photocatalytic degradation RhB, active substance capture tests and electron spin resonance (ESR) indicate that photo-cavities (h^+) and superoxide radicals ($\cdot O_2^-$) are active group and the hybrids reveal superior oxidation ability and remarkable visible-light harvesting owing to the direct Z-scheme heterojunction. In addition, the prominent performance of recyclability and stability reflect the capacious application prospects in the future.

Acknowledgement This work was supported by the National Natural Science Foundations of China (No. 11574138, 11874200 and 21427801), the Top-Notch Young Talents Program of China, the National Key R&D Program of China (2016YFA0201104) and Dengfeng Project B of Nanjing University. Thanks are due to Mr. Wang for assistance with writing and to Mr. Xu for valuable discussion.

References

1. P. Kumar, R. Boukherroub, K. Shankar, J. Mater. Chem. A. **6**(27), 12876–12931 (2018)
2. J. Yuan, X. Liu, Y. Liu, C. Liu, Y. Tang, Y. Zeng, L. Wang, S. Zhang, T. Cai, S. Luo, Y. Pei, Appl. Catal. B **237**, 24–31 (2018)
3. D. Zeng, P. Wu, W.-J. Ong, B. Tang, M. Wu, H. Zheng, Y. Chen, D.-L. Peng, Appl. Catal. B **233**, 26–34 (2018)

4. J. Fu, J. Yu, C. Jiang, B. Cheng, Adv. Energy Mater. **8**(3), 1701503 (2018)
5. S. Zeng, P. Kar, U.K. Thakur, K. Shankar, Nanotechnology **29**(5), 52001–052001 (2018)
6. K. Kamata, Bull. Chem. Soc. Jpn **92**(1), 133–151 (2019)
7. Y. Tan, Z. Shu, J. Zhou, T. Li, W. Wang, Z. Zhao, Appl. Catal. B **230**, 260–268 (2018)
8. Y. Wang, Q. Wang, X. Zhan, F. Wang, M. Safdar, J. He, Nanoscale **5**(18), 8326–8339 (2013)
9. W. Yu, D. Xu, T. Peng, J. Mater. Chem. A **3**(39), 19936–19947 (2015)
10. J. Wang, H. Shu, T. Zhao, P. Liang, N. Wang, D. Cao, X. Chen, Phys. Chem. Chem. Phys. **20**(27), 18571–18578 (2018)
11. Y. Cho, S. Kim, B. Park, C.-L. Lee, J.K. Kim, K.-S. Lee, I.Y. Choi, J.K. Kim, K. Zhang, S.H. Oh, J.H. Park, Nano Lett. **18**(7), 4257–4262 (2018)
12. W.J. Ong, L.L. Tan, Y.H. Ng, S.T. Yong, S.P. Chai, Chem. Rev. **116**(12), 7159–7329 (2016)
13. D. Xu, B. Cheng, W. Wang, C. Jiang, J. Yu, Appl. Catal. B **231**, 368–380 (2018)
14. B. Li, C. Lai, G. Zeng, L. Qin, H. Yi, D. Huang, C. Zhou, X. Liu, M. Cheng, P. Xu, C. Zhang, F. Huang, S. Liu, ACS Appl. Mater. Interfaces **10**(22), 18824–18836 (2018)
15. T. Di, B. Zhu, B. Cheng, J. Yu, J. Xu, J. Catal. **352**, 532–541 (2017)
16. J. Liu, B. Cheng, J. Yu, Phys. Chem. Chem. Phys. **18**(45), 31175–31183 (2016)
17. S. Mukherjee, S. Ganguly, K. Manna, S. Mondal, S. Mahapatra, D. Das, Inorg. Chem. **57**(7), 4050 (2018)
18. S. Chen, Y. Hu, S. Meng, X. Fu, Appl. Catal. B **150**, 564–573 (2014)
19. S. Imada, T. Kuraoka, E. Tokumitsu, H. Ishiwara, Jpn. J. Appl. Phys. **40**(2R), 666–671 (2001)
20. T. Li, L. Zhao, Y. He, J. Cai, M. Luo, J. Lin, Appl. Catal. B **129**, 255–263 (2013)
21. H. She, H. Zhou, L. Li, Z. Zhao, M. Jiang, J. Huang, L. Wang, Q. Wang, ACS Sustain. Chem. Eng. **7**(1), 650–659 (2019)
22. J. Wang, L. Tang, G. Zeng, Y. Liu, Y. Zhou, Y. Deng, J. Wang, B. Peng, ACS Sustain. Chem. Eng. **5**(1), 1062–1072 (2017)
23. Z. Jiang, W. Wan, H. Li, S. Yuan, H. Zhao, P.K. Wong, Adv. Mater. **30**(10), 1706108 (2018)
24. Q. Wang, W. Wang, L. Zhong, D. Liu, X. Cao, F. Cui, Appl. Catal. B **220**, 290–302 (2018)
25. Q. Xu, B. Zhu, C. Jiang, B. Cheng, J. Yu, Solar RrL. **2**(3), 1800006 (2018)
26. H. She, Y. Wang, H. Zhou, Y. Li, L. Wang, J. Huang, Q. Wang, ChemCatChem. **11**(2), 753–759 (2019)
27. A.S. Patra, G. Gogoi, R.K. Sahu, M. Qureshi, Phys. Chem. Chem. Phys. **19**(19), 12167–12174 (2017)
28. M. Jiang, Y. Shi, J. Huang, L. Wang, H. She, J. Tong, B. Su, Q. Wang, Eur. J. Inorg. Chem. **2018**(17), 1834–1841 (2018)
29. Q. Wang, Y. Shi, Z. Du, J. He, J. Zhong, L. Zhao, H. She, G. Liu, B. Su, Eur. J. Inorg. Chem. **2015**(24), 4108–4115 (2015)
30. S.-S. Yi, J.-M. Yan, B.-R. Wulan, S.-J. Li, K.-H. Liu, Q. Jiang, Appl. Catal. B **200**, 477–483 (2017)
31. S. Acharya, S. Mansingh, K.M. Parida, Inorg. Chem. Front. **4**(6), 1022–1032 (2017)
32. B. Luo, M. Chen, Z. Zhang, J. Xu, D. Li, D. Xu, W. Shi, Dalton T. **46**(26), 8431–8438 (2017)
33. X. Zhang, Y. Yang, W. Huang, Y. Yang, Y. Wang, C. He, N. Liu, M. Wu, L. Tang, Mater. Res. Bull. **99**, 349–358 (2018)
34. J. Luo, X. Zhou, X. Ning, L. Zhan, J. Chen, Z. Li, Sep. Purif. Technol. **201**, 327–335 (2018)
35. Q. Wang, Y. Shi, L. Pu, Y. Ta, J. He, S. Zhang, J. Zhong, J. Li, B. Su, Appl. Surf. Sci. **367**, 109–117 (2016)
36. J. Chu, X. Han, Z. Yu, Y. Du, B. Song, P. Xu, ACS Appl. Mater. Interfaces **10**(24), 20404–20411 (2018)
37. S. Tonda, S. Kumar, M. Bhardwaj, P. Yadav, S. Ogale, ACS Appl. Mater. Interfaces **10**(3), 2667–2678 (2018)
38. A.T. Kozakov, A.G. Kochur, A.V. Nikolsky, K.A. Googlev, V.G. Smotrakov, V.V. Eremkin, J Electron Spectros Relat Phenomena. **184**, 508–516 (2011)
39. A.G. Kochur, A.T. Kozakov, K.A. Googlev, A.V. Nikolskii, J Electron Spectros Relat Phenomena. **195**, 1–7 (2014)
40. Z. Zhang, C. Shao, X. Li, C. Wang, M. Zhang, Y. Liu, ACS Appl. Mater. Interfaces. **2**(10), 2915–2923 (2010)
41. L. Ge, C. Han, X. Xiao, L. Guo, Int. J. Hydrogen Energy **38**(17), 6960–6969 (2013)
42. S. Zhuo, M. Shao, S.T. Lee, ACS Nano **6**(2), 1059–1064 (2012)
43. L. Zhang, W. Yu, C. Han, J. Guo, Q.H. Zhang, H.Y. Xie, Q. Shao, Z.G. Sun, Z.H. Guo, J. Electrochem. Soc. **164**(9), H651–H656 (2017)
44. X. Jiao, Z. Chen, X. Li, Y. Sun, S. Gao, W. Yan, C. Wang, Q. Zhang, Y. Lin, Y. Luo, Y. Xie, J. Am. Chem. Soc. **139**(22), 7586–7594 (2017)
45. L. Liao, J. Zhu, X. Bian, L. Zhu, M.D. Scanlon, H.H. Girault, B. Liu, Adv. Funct. Mater. **23**(42), 5326–5333 (2013)
46. L. Qian, L. Gu, L. Yang, H. Yuan, D. Xiao, Nanoscale **5**(16), 7388–7396 (2013)
47. J. Wang, Y. Wang, W. Yang, X. Chen, Y. Zhu, Appl. Catal. B **220**, 337–347 (2018)
48. L.Q. Ye, C.Q. Han, Z.Y. Ma, Y.M. Leng, J. Li, X.X. Ji, D.Q. Bi, H.Q. Xie, Z.X. Huang, Chem. Eng. J. **307**, 311–318 (2017)
49. H. Zhao, P. Jiang, W. Cai, Chem. Asian J. **12**(3), 361–365 (2017)
50. H. Yu, B. Huang, H. Wang, X. Yuan, L. Jiang, Z. Wu, J. Zhang, G. Zeng, J. Colloid Interface Sci. **522**, 82–94 (2018)
51. A. Fujishima, X. Zhang, D. Tryk, Surf. Sci. Rep. **63**(12), 515–582 (2008)
52. S.C. Yan, Z.S. Li, Z.G. Zou, Langmuir **25**(17), 10397–10401 (2009)
53. J.H. Pasch, J.H. Elbe, J. Food Sci. **44**(1), 72–75 (1979)
54. C.-C. Pan, J.C.S. Wu, Mater. Chem. Phys. **100**(1), 102–107 (2006)
55. X.J. Chen, Y.Z. Dai, X.Y. Wang, G. Jing, T.H. Liu, F.F. Li, J. Hazard. Mater. **292**, 9–18 (2015)
56. Y. Gong, X. Zhao, J. Zhang, H. Zhang, B. Yang, K. Xiao, T. Guo, H. Shao, Y. Wang, G. Yu, Appl. Catal. B **233**, 35–45 (2018)
57. Y.-F. Zhang, L.-G. Qiu, Y.-P. Yuan, Y.-J. Zhu, X. Jiang, J.-D. Xiao, Appl. Catal. B **144**, 863–869 (2014)
58. Z. Xie, Y. Feng, F. Wang, D. Chen, Q. Zhang, Y. Zeng, W. Lv, G. Liu, Appl. Catal. B **229**, 96–104 (2018)
59. N.I.M. Rosli, S.M. Lam, J.C. Sin, I. Satoshi, A.R. Mohamed, J. Environ. Eng. **144**(2), 04017091 (2018)
60. W.-D. Oh, V.W.C. Chang, Z.-T. Hu, R. Goei, T.-T. Lim, Chem. Eng. J. **323**, 260–269 (2017)
61. M.R. Hoffmann, S.T. Martin, W. Choi, D.W. Bahnemann, Chem. Rev. **95**(1), 69–96 (1995)
62. I. Tateishi, H. Katsumata, T. Suzuki, S. Kaneco, Mater. Lett. **201**, 66–69 (2017)
63. S.F. Wang, H. Yang, T. Xian, X.Q. Liu, Catal. Commun. **12**(7), 625–628 (2011)
64. J. Luo, X. Zhou, L. Ma, X. Xu, Appl. Surf. Sci. **390**, 357–367 (2016)
65. R.G. Pearson, Inorg. Chem. **27**(4), 734–740 (1988)
66. C. Chen, W. Cai, M. Long, B. Zhou, Y. Wu, D. Wu, Y. Feng, ACS Nano **4**(11), 6425–6432 (2010)